Supporting Information for: Surface enrichment dictates block copolymer orientation

Suwon Bae and Kevin G. Yager*

Center for Functional Nanomaterials, Brookhaven National Laboratory, Upton, New York 11973, United States

Marcus M. Noack

The Center for Advanced Mathematics for Energy Research Applications, Lawrence Berkeley National Laboratory, Berkeley, California 94720, United States

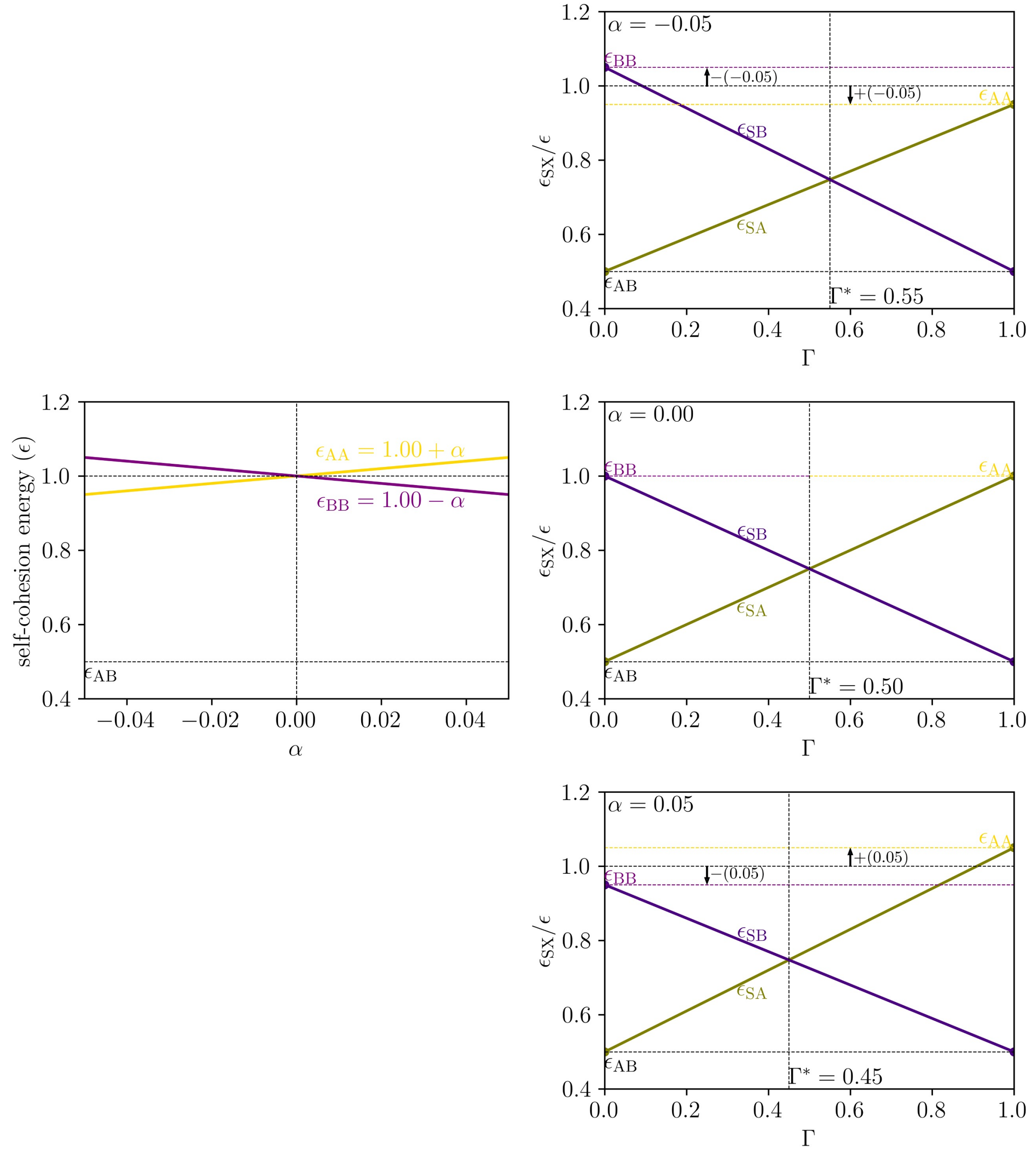

Figure S1: Parameters for our molecular dynamics (MD) model representing an A-*b*-B block copolymer (BCP) film on top of a substrate (type S). (left) The self-cohesion energies between like beads (ϵ_{AA} and ϵ_{BB}) are defined using the parameter α and (right) the strengths of non-bonded interactions (ϵ_{SA} and ϵ_{SB}) between substrate beads and BCP chain beads are parameterized using a linear dependence on Γ. ϵ_{SA} and ϵ_{SB} are also dependent on ϵ_{AA} and ϵ_{BB}, since these are used as the limiting values (three different α are shown as examples). The parameter Γ can be interpreted as the substrate composition; i.e. it has interactions expected for a substrate-attached brush of A-*r*-B random copolymer with composition Γ. It is at $\Gamma = \Gamma^*$ that the interaction strengths with the two blocks are equal.

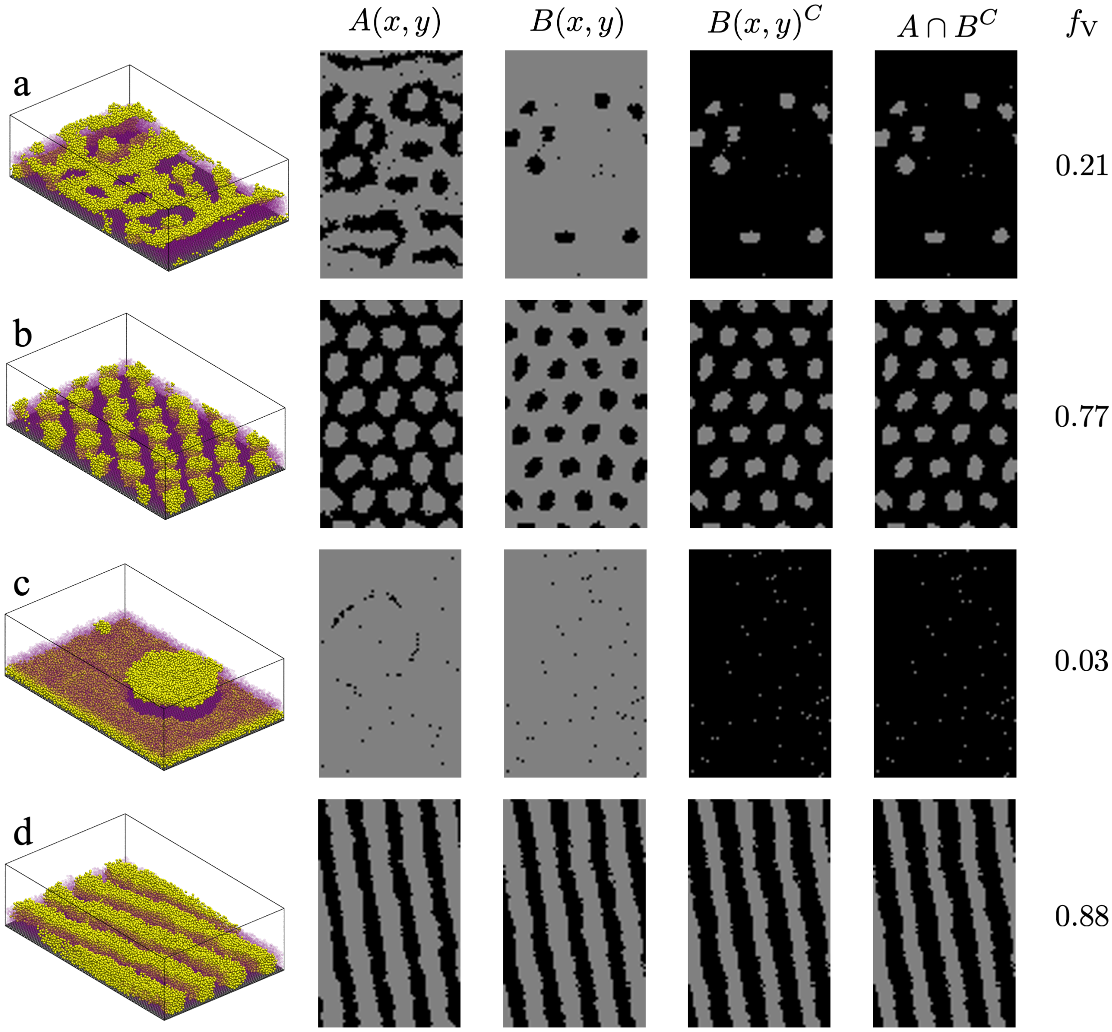

Figure S2: Method for computing the vertical fraction (f_V). Examples are provided for four different films (a-d) presented in Figure 2 in the manuscript. The calculation is based on the projected spatial distribution (along z direction) of the blocks through the 3D film volume (MD perspective view shown on left). Spatial maps of the A (minority) and B (majority/matrix) domains are computed. The A map visualizes all (x, y) locations where any A material appears. We then compute the complement of B (B^C) which yields all locations without any B. The intersection of these ($A \cap B^C$) yields all locations where only A appears; which indicates that the A block persists from the top to the bottom of the film (i.e. the morphology is vertical at that location). The normalized sum of such a map provides an estimate for f_V.

Anisotropic and symmetric kernel

For Gaussian process (GP) modeling of the parameter space, we used an anisotropic kernel, which has different correlation length for different directions in the space. Our aniostropic kernel function can be written as

$$k(\mathbf{x}^m, \mathbf{x}^n) = \sigma_s^2 \exp\left[-\left(\sum_i^d \frac{|x_i^m - x_i^n|^2}{\phi_i^2}\right)^{1/2}\right] \tag{S1}$$

where the superscripts m, n refer to m-th and n-th components of $\mathbf{x}$, the subscript i stands for different directions, d is the dimensionality of the space ($d = 3$ in this work), σ_s^2 is signal variance, and ϕ_i is the hyperparameter for the i direction. In our study, $i = 1$, 2, and 3 correspond to f_A, α, and Γ.

The parameter space exhibits several known symmetries, which are captured by:

$$M(f_\mathrm{A}, \alpha, \Gamma) = M(1 - f_\mathrm{A}, -\alpha, 1 - \Gamma)$$

In particular, a material of composition f_A should exhibit the same bulk morphology as composition $1 - f_\mathrm{A}$. E.g. one observes cylinders at $f_\mathrm{A} = 0.25$ and inverse cylinders at $f_\mathrm{A} = 0.75$. Identical thin film behavior will be observed only if the corresponding interfacial energies are the same, which requires swapping surface tensions ($\alpha \to -\alpha$) and correspondingly inverting substrate energy ($\Gamma \to 1-\Gamma$). Thus, the space exhibits point symmetry about $(0.5, 0, 0.5)$. Rewritten in the abstract notation of our GP kernel:

$$M(x_1, x_2, x_3) = M(0.5 + (0.5 - x_1), -x_2, 0.5 + (0.5 - x_3))$$

To implement these symmetries into the anisotropic kernel, we separate the distance term in Equation S1 into 4 terms as follows:

$$\begin{aligned} k(\mathbf{x}^m, \mathbf{x}^n) = \frac{\sigma_s^2}{4}\Bigg\{ &\exp\left[-\left(\sum_i^d \frac{|x_i^m - x_i^n|^2}{\phi_i^2}\right)^{1/2}\right] \\ &+\exp\left[-\left(\sum_i^d \frac{|{}^-x_i^m - x_i^n|^2}{\phi_i^2}\right)^{1/2}\right] \\ &+\exp\left[-\left(\sum_i^d \frac{|x_i^m - {}^-x_i^n|^2}{\phi_i^2}\right)^{1/2}\right] \\ &+\exp\left[-\left(\sum_i^d \frac{|{}^-x_i^m - {}^-x_i^n|^2}{\phi_i^2}\right)^{1/2}\right]\Bigg\} \end{aligned} \tag{S2}$$

where ${}^-x_i$ is defined as:

$$\begin{aligned} {}^-x_1^j &= \begin{cases} 0.5 + (0.5 - x_1^j) & \text{if } x_1^j \leq 0.5 \\ x_1^j & \text{if } x_1^j > 0.5 \end{cases} \\ {}^-x_2^j &= \begin{cases} -x_2^j & \text{if } x_1^j \leq 0.5 \\ x_2^j & \text{if } x_1^j > 0.5 \end{cases} \\ {}^-x_3^j &= \begin{cases} 0.5 + (0.5 - x_3^j) & \text{if } x_1^j \leq 0.5 \\ x_3^j & \text{if } x_1^j > 0.5 \end{cases} \end{aligned}$$

Data acquisition function

Carrying out the GP regression model results in hyperparameters σ_s, ϕ_1, ϕ_2, and ϕ_3 that maximize the marginal log-likelihood of the regression model. Using the trained surrogate model, a data acquisition function can be used to guide the parameter space exploration by selecting which subsequent point to measure (or in this case, what simulation to compute). While we can technically explore the whole space, we are most interested in understanding the behavior of the vertical morphology, and thus wish to focus data-collection to identify the boundary of the vertical region. To achieve this, we utilized the following data acquisition function:

$$f(\mathbf{x}) = \sqrt{\sigma(\mathbf{x})^2} - |m(\mathbf{x}) - 0.8| \tag{S3}$$

where $\sigma(\mathbf{x})^2$ is the posterior covariance and $m(\mathbf{x})$ is the posterior mean at point $\mathbf{x}$.

The next point to observe, $\hat{\mathbf{x}}$, is found by maximizing the data acquisition function. The acquisition function is maximized when the first term is large and the second term close to zero, meaning that at the suggested point the posterior mean is comparable to 0.8 and the posterior variance, or error, is large. By incorporating the posterior covariance into the acquisition function, a point where we see the largest uncertainty is chosen among points where the posterior mean is about 0.8. Thus, this acquisition function naturally concentrates data collection in regions where $f_{\mathrm{V}} \approx 0.8$ (i.e. the transition boundary between vertical and horizontal orientations), while also distributing points throughout the space so as to reduce model uncertainty. This allows us to efficiently sample the space, and converge to a high-quality surrogate model with few simulation runs.

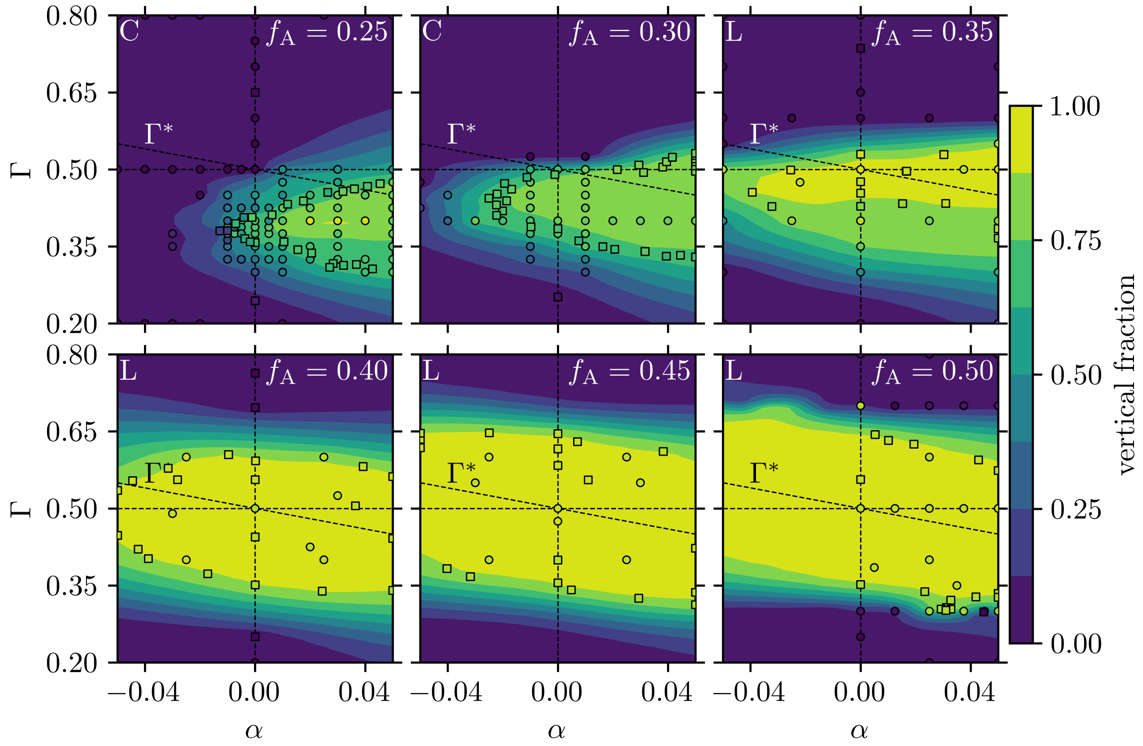

Figure S3: Two-dimensional slices through the full parameter space, using false color to denote morphology orientation. The 359 "measured points" (simulations performed for these conditions) are shown by the points; circles denote points manually selected by the human researchers, while square symbols denote points selected by the autonomous loop, using Gaussian process modeling. The false color map is based on the trained GP model, using a symmetric, anisotropic kernel. The best-fit hyperparamters are $\sigma_s^2 = 0.635$, $\phi_1 = \phi_{f_A} = 0.418$, $\phi_2 = \phi_\alpha = 0.328$, $\phi_3 = \phi_\Gamma = 0.435$.

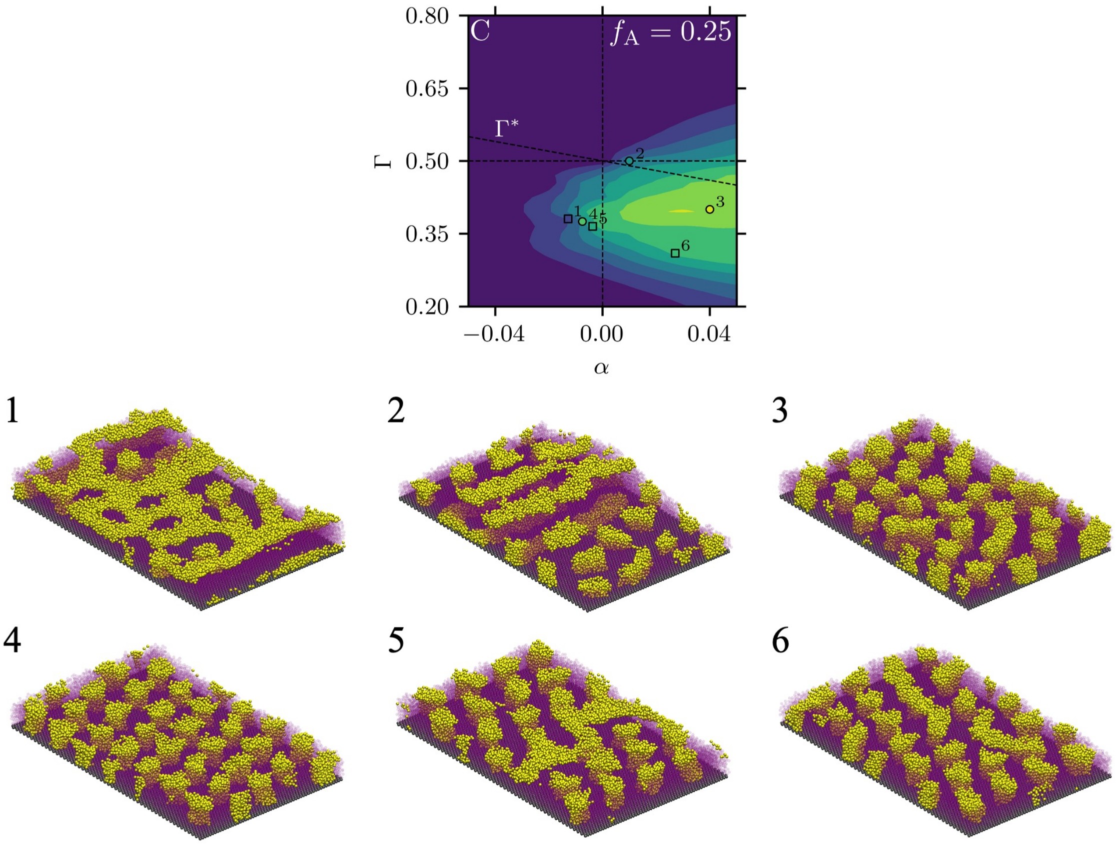

Figure S4: Two-dimensional slice through the full parameter space, at $f_A = 0.25$. The morphologies at select points (given in Table S1) are highlighted.

Table S1: Values for parameters α and Γ, and computed vertical fraction (f_V), for the morphologies shown in Figure S4 (i.e. at $f_A = 0.25$).

	1	2	3	4	5	6
α	-0.013	0.010	0.040	-0.008	-0.004	0.027
Γ	0.381	0.500	0.400	0.375	0.365	0.310
f_V	0.21	0.51	0.93	0.72	0.61	0.68

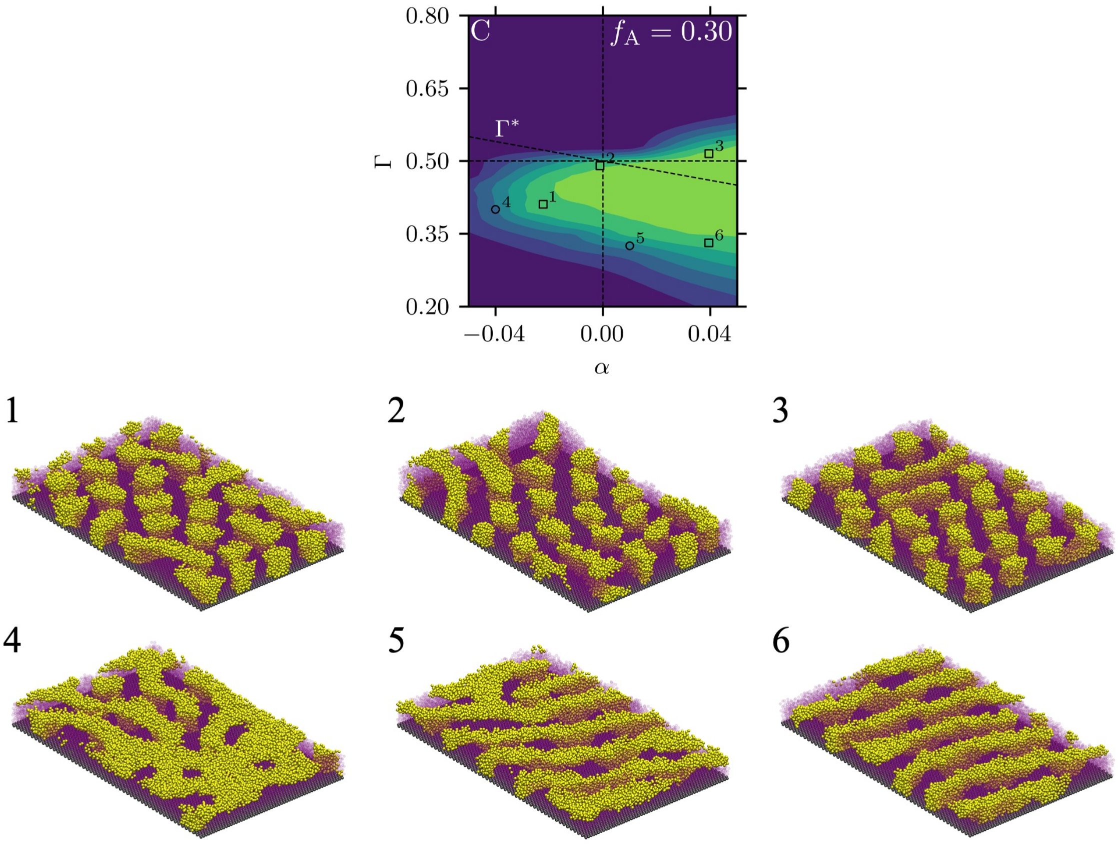

Figure S5: Two-dimensional slice through the full parameter space, at $f_{\mathrm{A}} = 0.30$. The morphologies at select points (given in Table S2) are highlighted.

Table S2: Values for parameters α and Γ, and computed vertical fraction (f_{V}), for the morphologies shown in Figure S5 (i.e. at $f_{\mathrm{A}} = 0.30$).

	1	2	3	4	5	6
α	-0.022	-0.001	0.039	-0.040	0.010	0.039
Γ	0.411	0.490	0.515	0.400	0.422	0.331
f_{V}	0.71	0.73	0.81	0.31	0.42	0.65

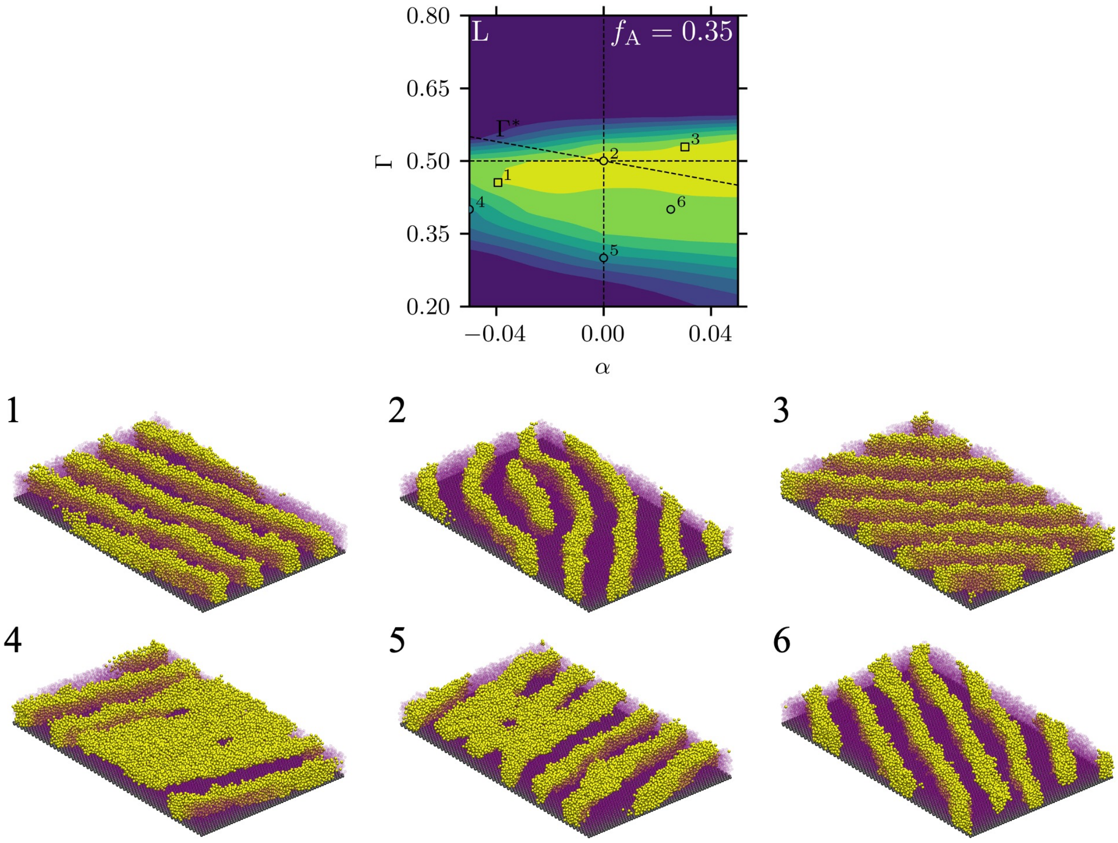

Figure S6: Two-dimensional slice through the full parameter space, at $f_A = 0.35$. The morphologies at select points (given in Table S3) are highlighted.

Table S3: Values for parameters α and Γ, and computed vertical fraction (f_V), for the morphologies shown in Figure S6 (i.e. at $f_A = 0.35$).

	1	2	3	4	5	6
α	-0.039	0.000	0.030	-0.050	0.000	0.025
Γ	0.456	0.500	0.529	0.400	0.300	0.400
f_V	0.92	0.94	0.93	0.45	0.48	0.79

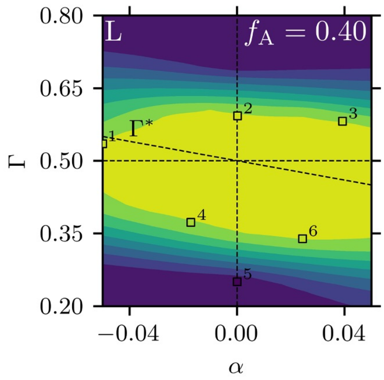

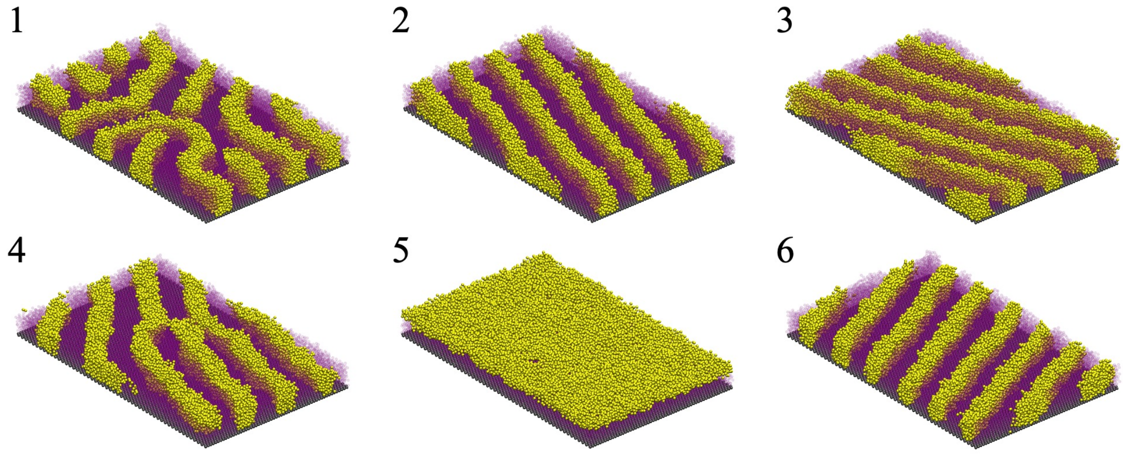

Figure S7: Two-dimensional slice through the full parameter space, at $f_A = 0.40$. The morphologies at select points (given in Table S4) are highlighted.

Table S4: Values for parameters α and Γ, and computed vertical fraction (f_V), for the morphologies shown in Figure S7 (i.e. at $f_A = 0.40$).

	1	2	3	4	5	6
α	-0.050	0.000	0.039	-0.017	0.000	0.024
Γ	0.535	0.593	0.582	0.373	0.250	0.339
f_V	0.91	0.93	0.91	0.87	0.01	0.90

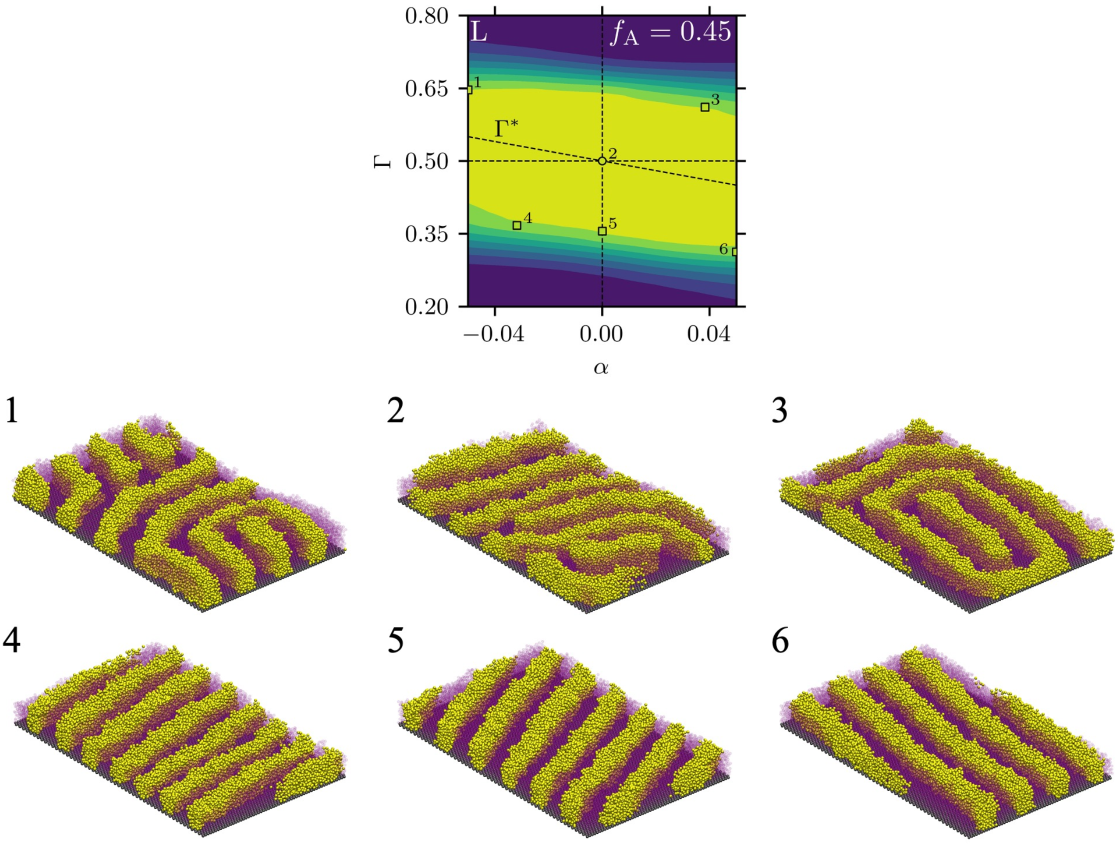

Figure S8: Two-dimensional slice through the full parameter space, at $f_A = 0.45$. The morphologies at select points (given in Table S5) are highlighted.

Table S5: Values for parameters α and Γ, and computed vertical fraction (f_V), for the morphologies shown in Figure S8 (i.e. at $f_A = 0.45$).

	1	2	3	4	5	6
α	-0.050	0.000	0.038	-0.032	0.000	0.050
Γ	0.647	0.500	0.611	0.367	0.355	0.313
f_V	0.91	0.92	0.90	0.88	0.88	0.88

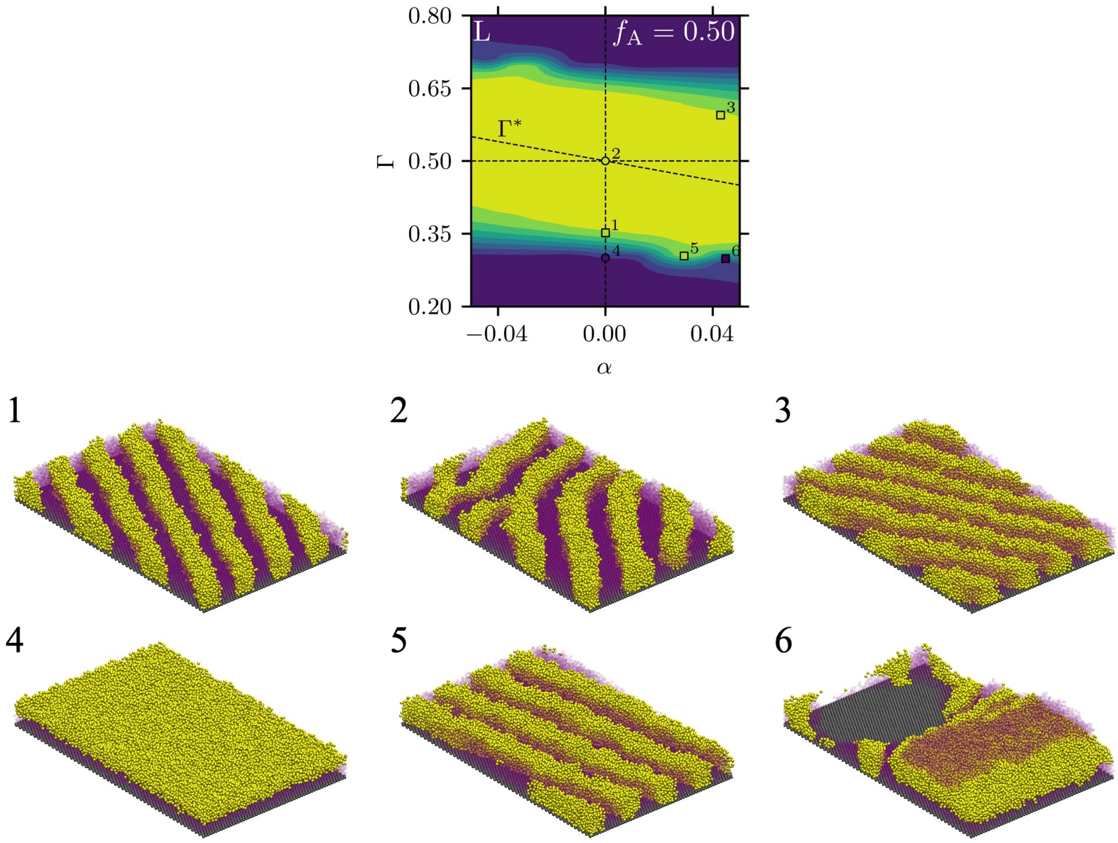

Figure S9: Two-dimensional slice through the full parameter space, at $f_A = 0.50$. The morphologies at select points (given in Table S6) are highlighted.

Table S6: Values for parameters α and Γ, and computed vertical fraction (f_V), for the morphologies shown in Figure S9 (i.e. at $f_A = 0.50$).

	1	2	3	4	5	6
α	0.000	0.000	0.043	0.000	0.029	0.045
Γ	0.352	0.500	0.595	0.300	0.304	0.299
f_V	0.88	0.91	0.90	0.05	0.87	0.00

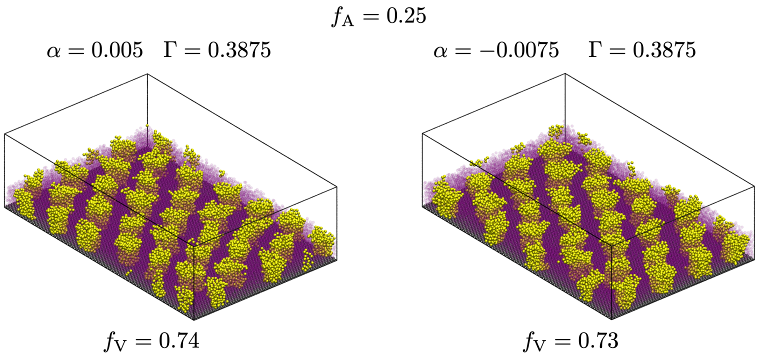

Figure S10: Morphologies formed by cylindrical pBCP (left) and nBCP (right) look similar and exhibit comparable vertical fractions. Minority A blocks are colored yellow and majority B blocks purple, regardless of α.

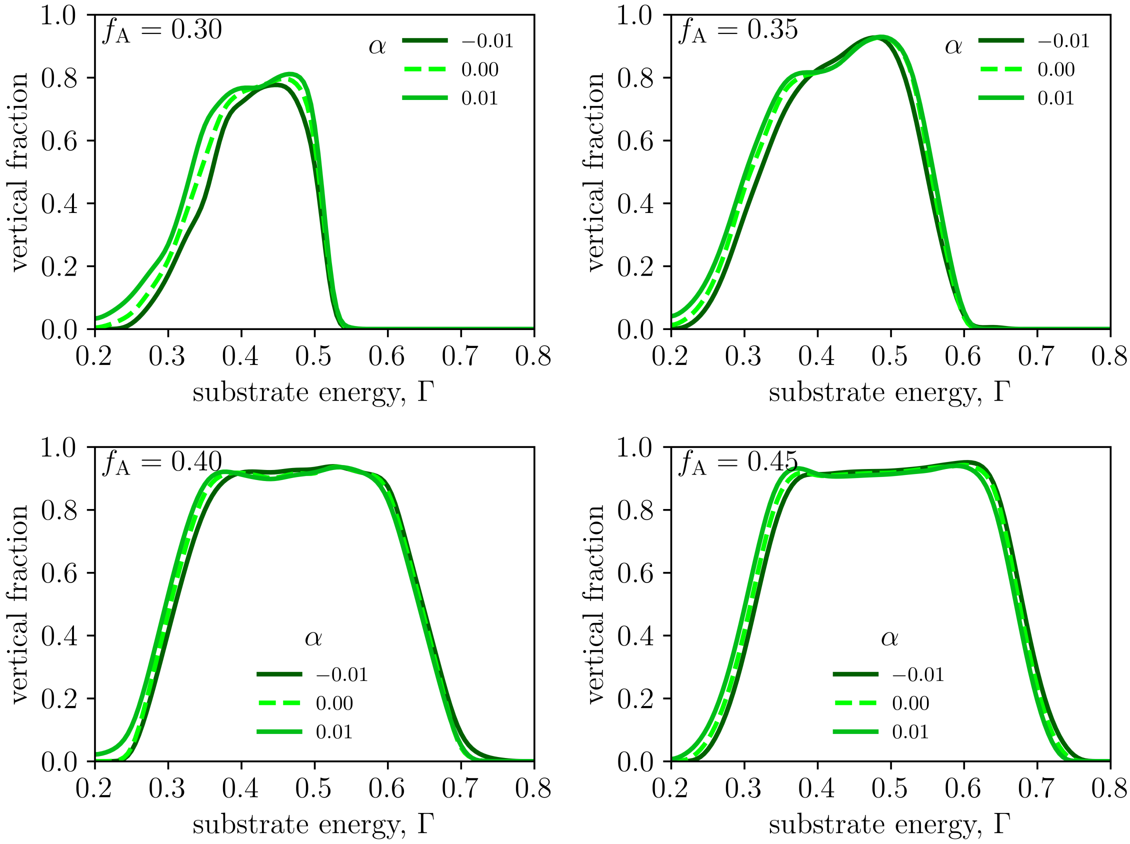

Figure S11: Differences between pBCP and nBCP for various f_A when $|\alpha| = 0.01$. The difference between pBCP and nBCP is small for $f_\mathrm{A} > 0.25$ (and indeed α makes no difference for $f_\mathrm{A} = 0.5$). However, at $f_\mathrm{A} = 0.25$ (see main text), α has a substantial effect.

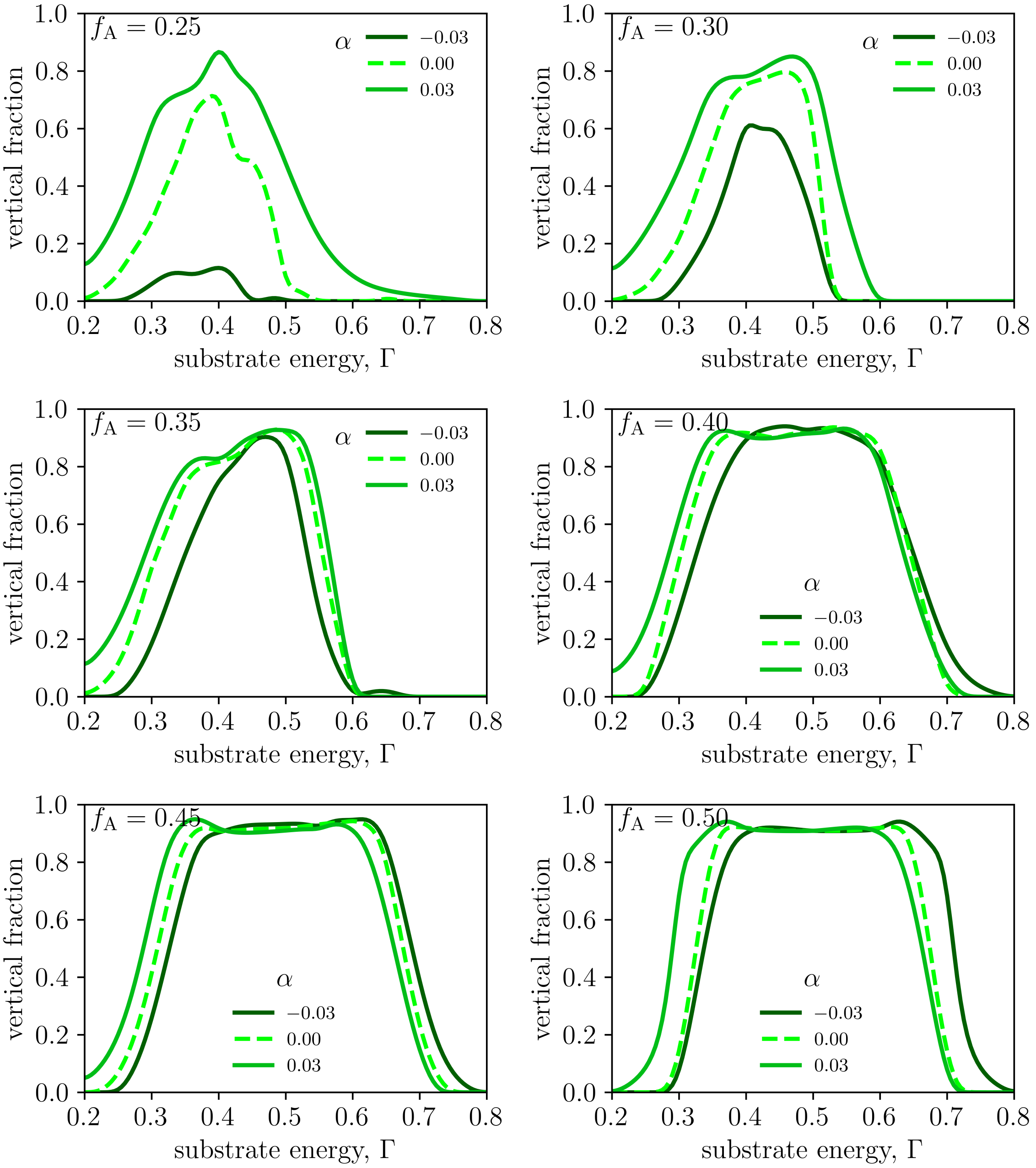

Figure S12: Differences between pBCP and nBCP for various f_A when $|\alpha| = 0.03$. The differences are more pronounced as $|\alpha|$ increases, and as f_A decreases.

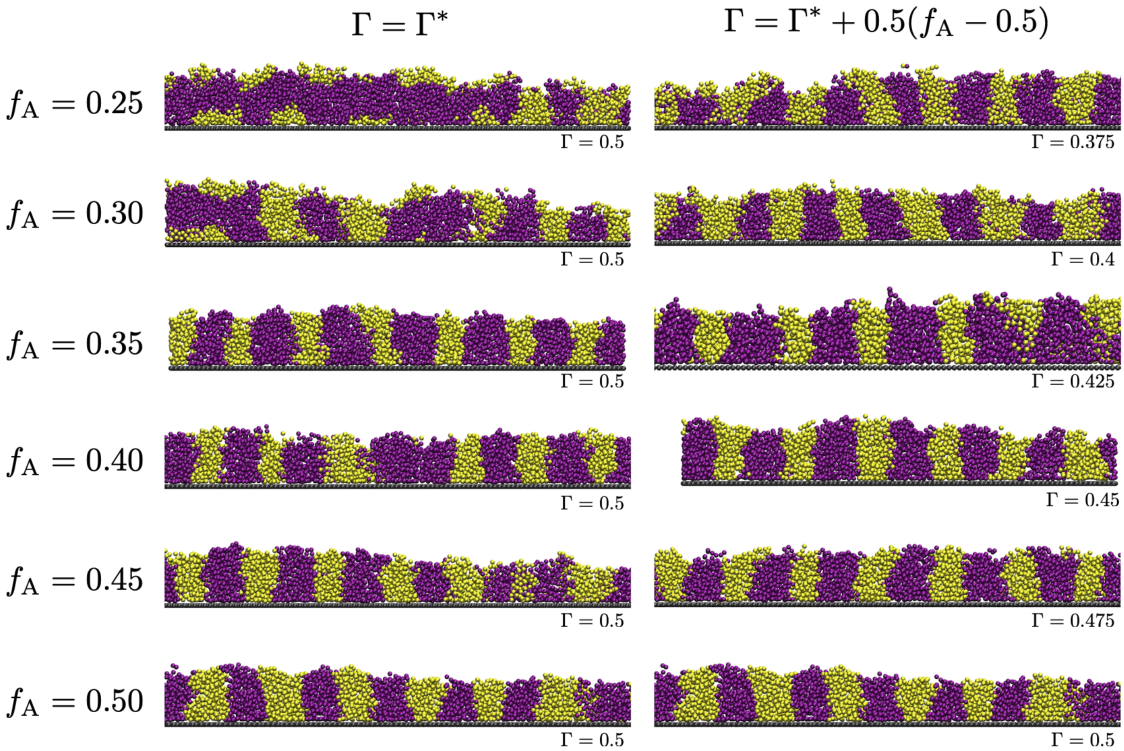

Figure S13: Cross-sectional molecular snapshots of BCP films on two different kinds of substrates for various f_A ($\alpha = 0$ throughout). Cylinder-forming BCPs barely or partly form vertical cylinders on $\Gamma = \Gamma^*$ while lamella-forming ones exhibit vertical structures. Substrates with $\Gamma = \Gamma^* + 0.5(f_\mathrm{A} - 0.5)$ neutralizes the enrichment of A blocks at the interfaces for $f_\mathrm{A} = 0.25$ and 0.3 and thus promotes vertical morphologies. Presented data is at $T = 1.2\epsilon/k_\mathrm{B}$ (before final equilibration at $T = 0.8\epsilon/k_\mathrm{B}$).

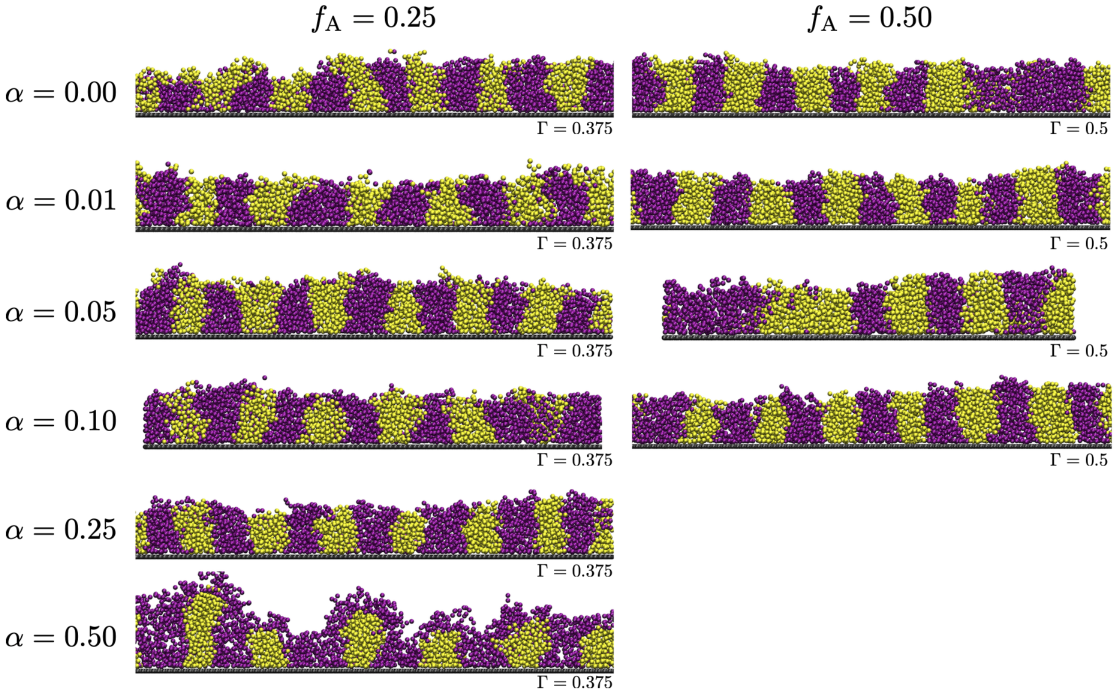

Figure S14: Cross-sectional molecular snapshots of vertical cylinders ($f_A = 0.25$) and lamellae ($f_A = 0.5$) for various α. Consistent with the associated density curves (Figure 6 in main text), vertical morphologies on average swell in the middle (thin film midplane) as α increases. This occurs because the higher surface tension of the minority block causes this material (A beads) to recede from interfaces. The enrichment of A block material in the film interior thus increases with increasing α (c.f. Figure S15). For extreme surface tension disparity ($\alpha = 0.50$), the morphology is strongly disrupted as the system rearranges in order to coat the entire film surface in the lower surface tension B matrix. Presented data is at $T = 1.2\epsilon/k_B$ (before final equilibration at $T = 0.8\epsilon/k_B$).

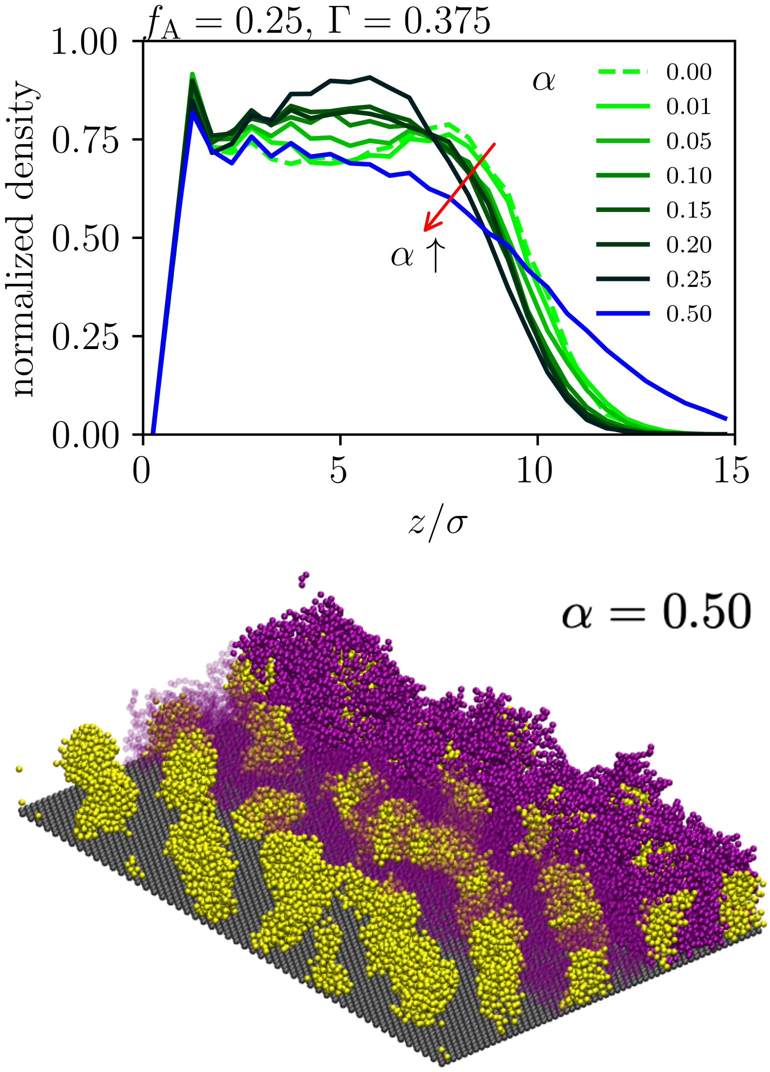

Figure S15: The response of vertical cylinders to surface tension disparity, α. As the disparity increases, more A material is concentrated towards the middle of the film (away from interfaces), causing the corresponding vertical cylinder object to bulge. For extreme surface tension disparity (α), the morphology is disrupted as the matrix B material coats the entire film-vacuum interface. Presented data is at $T = 1.2\epsilon/k_B$ (before final equilibration at $T = 0.8\epsilon/k_B$).

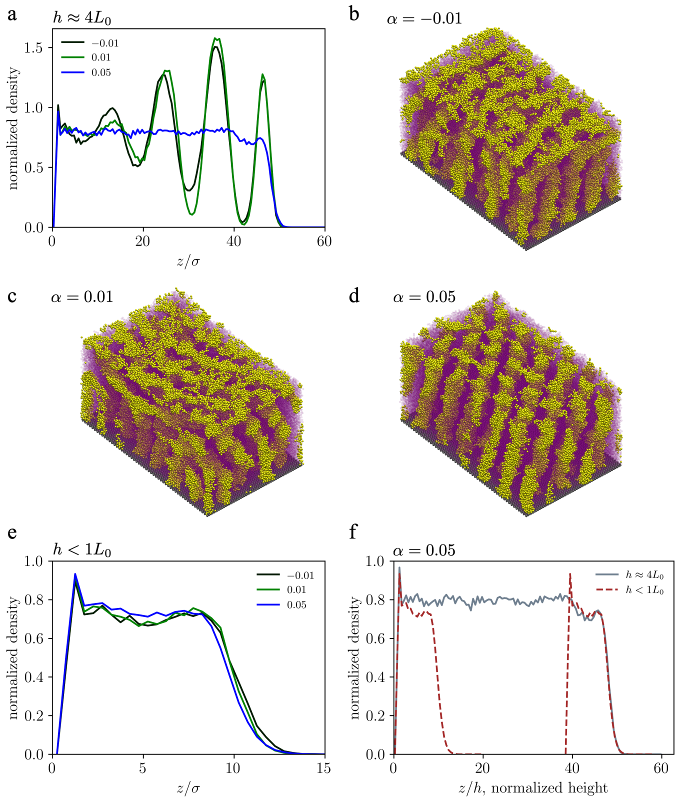

Figure S16: (a) Density of minority A beads through the thickness of thicker ($h \approx 4L_0$) films of cylinder-forming material ($f_A = 0.25$), along with (b-d) morphology visualization. Despite the neutral substrate condition ($\Gamma = 0.4$), a vertical orientation is more difficult to achieve in thick films than thin films (e) since interface-directed ordering must propagate over greater distances. Nevertheless, simulations in thicker films confirm results in thinner films, where larger positive α tends to stabilize the vertical orientation. (f) Moreover, ordering near interfaces of a thick film is similar to that observed in a thin film.

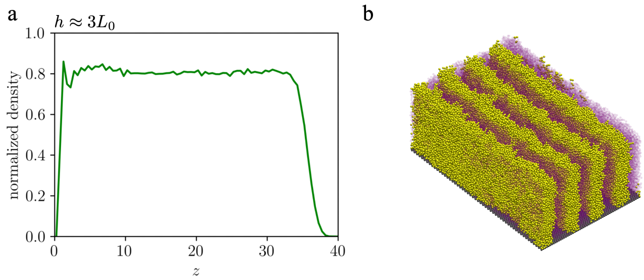

Figure S17: (a) Density of A beads and (b) morphology for a thicker film ($h \approx 3L_0$) of lamellae-forming material ($f_A = 0.5$).